Low-temperature co-purification of NO_x and Hg^0 from simulated flue gas by $Ce_xZr_yMn_zO_2$/r-Al_2O_3: the performance and its mechanism

By: Pei Lu, Huifang Yue, Yi Xing, Jianjun Wei, Zheng Zeng, Rui Li, and Wanrong Wu

P. Lu, H. Yue, Y. Xing, J. Wei, Z. Zeng, R. Li, W. Wu, Low-temperature co-purification of NO_x and Hg^0 from simulated flue gas by $Ce_xZr_yMn_zO_2$/r-Al_2O_3: the performance and its mechanism, *Environmental Science and Pollution Research*, **2018** 25 (21), 20575-20590. DOI: 10.1007/s11356-018-2199-4.

Abstract:

In this study, series of $Ce_xZr_yMn_zO_2$/r-Al_2O_3 catalysts were prepared by impregnation method and explored to co-purification of NO_x and Hg^0 at low temperature. The physical and chemical properties of the catalysts were investigated by XRD, BET, FTIR, NH_3-TPD, H_2-TPR, and XPS. The experimental results showed that 10% $Ce_{0.2}Zr_{0.3}Mn_{0.5}O_2$/r-$Al_2O_3$ yielded higher conversion on co-purification of NO_x and Hg^0 than the other prepared catalysts at low temperature, especially at 200–300 °C. 91% and 97% convert rate of NO_x and Hg^0 were obtained, respectively, when 10% $Ce_{0.2}Zr_{0.3}Mn_{0.5}O_2$/r-$Al_2O_3$ catalyst was used at 250 °C. Moreover, the presence of H_2O slightly decreased the removal of NO_x and Hg^0 owing to the competitive adsorption of H_2O and Hg^0. When SO_2 was added, the removal of Hg^0 first increased slightly and then presented a decrease due to the generation of SO_3 and $(NH_4)_2SO_4$. The results of NH_3-TPD indicated that the strong acid of 10% $Ce_{0.2}Zr_{0.3}Mn_{0.5}O_2$/r-$Al_2O_3$ improved its high-temperature activity. XPS and H_2-TPR results showed there were high-valence Mn and Ce species in 10% $Ce_{0.2}Zr_{0.3}Mn_{0.5}O_2$/r-$Al_2O_3$, which could effectively promote the removal of NO_x and Hg^0. Therefore, the mechanisms of Hg^0 and NO_x removal were proposed as Hg (ad) + [O] → HgO (ad), and $2NH_3/NH_4^+$ (ad) + NO_2 (ad) + NO (g) → 2 N_2 + $3H_2O/2H^+$, respectively.

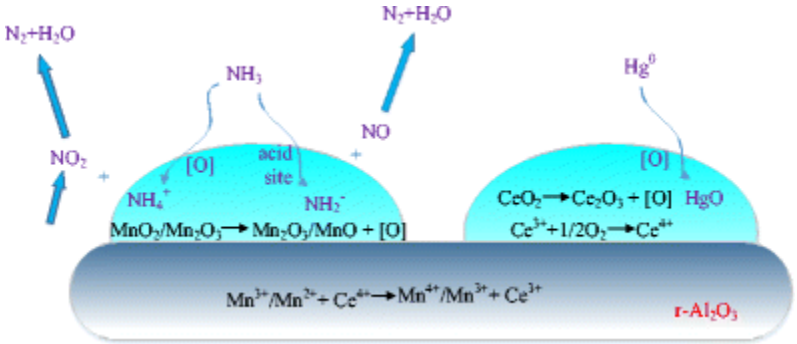

Keywords: Low temperature | Co-purification | NO_x and Hg^0 | $Ce_{0.2}Zr_{0.3}Mn_{0.5}O_2$ | Performance and mechanism

Article:

Introduction

Up to now, the burning of coal releases large amounts of nitrogen oxides (NO_x) and elemental mercury (Hg^0) into the atmosphere, especially in China (Yu et al. 2017; Hu et al. 2015). NO_x leads to global climate change, but it also causes haze, acid rain, and other secondary pollution (Zhao et al. 2015). Hg^0 has caused great harm to humans and the environment because of its high volatility, long persistence, and strong bioaccumulation properties (Zhang et al. 2017). NO_x and Hg^0 are extremely harmful to the human body, and as major pollutants, they urgently need to be controlled (Li et al. 2017; He et al. 2016).

Various methods and techniques have been implemented to control NO_x and Hg^0 emissions (Yang et al. 2015; He et al. 2014; Liu et al. 2016, 2017, 2018), such as selective catalytic reduction (SCR) and activated carbon injection (ACI) (Yang et al. 2015; Karami and Salehi 2012; Rallo et al. 2012). However, simultaneous removal of NO_x and Hg^0 is more attractive to researchers and society in general (Fernández-Miranda et al. 2016; Zhao et al. 2015; Li et al. 2015; Wang et al. 2015). Recently, studies have shown that catalysts for SCR of NO_x can promote oxidation of Hg^0 (Fernández-Miranda et al. 2016). Therefore, low-cost SCR is one of the most promising ways to simultaneously remove NO_x and Hg^0 (Zhao et al. 2015; Li et al. 2015).

However, the operating temperature of SCR is usually above 300 °C in terms of obtaining good catalytic activity (Li et al. 2011; Benson et al. 2005). However, it will limit the physical adsorption of Hg^0 and increase operating costs, hindering the application of SCR technology (Zhou et al. 2016a; Presto and Granite 2006). The conventional carrier for conventional SCR catalysts is TiO_2. TiO_2 has a low specific surface area and a poor thermal stability, which limits its application in the SCR technology (Zhang et al. 2015). Therefore, it is necessary to develop efficient SCR catalysts with high specific surface area that could be applied at low temperature. Scientists have carried out many innovative studies on low-temperature catalytic removal of NO_x and Hg^0 (Zhao et al. 2015; Li et al. 2015; Wang et al. 2015), including optimizing the synthesis method and optimizing the components of the catalyst to improve its performance (low-temperature activity and stability). The method of optimizing the catalyst composition is easier and safer than the synthesis, attracting many researchers (Li et al. 2011; Guo et al. 2014). Additionally, the working temperature of the SCR catalyst can be reduced by doping metal or metal oxide in the carrier, which increases catalytic reduction efficiency (Deng et al. 2014; Gunnarsson et al. 2015; Cao et al. 2015; Zhao et al. 2015).

The r-Al_2O_3 substrate has been used by many researchers as a carrier of SCR because of its large surface area and good stability (Cao et al. 2015; Zhao et al. 2015; Qu et al. 2014). In addition, MnO_x has different types of oxygen that can complete the catalytic cycle (Shen et al. 2013; Chen et al. 2012), and MnO_x has high activity for low-temperature SCR of NO, associated with different Mn valence states (Su et al. 2013; Kima et al. 2010; Wu et al. 2007). However, when

directly exposed to a SO_2 atmosphere, MnO_2 is easily vulcanized, causing catalyst poisoning (Jin et al. 2014; Wang et al. 2013). CeO_2 has excellent oxygen storage and redox properties and is used to improve the SCR activity and resistance to SO_2 (Zhang et al. 2012; Chang et al. 2012; Wang et al. 2014). In fact, the CeO_2-based catalysts have been deeply discussed on the research of removing NO_x and mercury. Meanwhile, the incorporation of other metal oxides into the CeO_2 lattice is generally considered to achieve better redox and sulfur resistance of catalyst (Xu et al. 2008; Du et al. 2012). In addition, Mn-Ce mixed oxides have excellent low-temperature mercury removal performance (Yang et al. 2017a). Moreover, studies have shown that the introduction of Zr into CeO_2 can increase the lattice oxygen transfer rate and improve the quality of redox reactions (Esteves et al. 2011; Kim et al. 2012). Therefore, with $Ce_aZr_bMn_cO_x$ as the active ingredient and r-Al_2O_3 as the substrate, simultaneous removal NO_x and Hg^0 is promising. However, few studies have studied $Ce_aZr_bMn_cO_x$/r-Al_2O_3 for low-temperature simultaneous removal of NO_x and Hg^0, and the mechanism for simultaneous removal of NO_x and Hg^0 rarely been reported.

Therefore, in order to understand the catalytic mechanism of simultaneous removal of NO and Hg^0 and the roles of SO_2 and H_2O properties on the function and lifetime of the catalyst, $Ce_xZr_yMn_zO_2$/r-Al_2O_3 was synthesized and characterized by X-ray diffraction (XRD), Brunauer-Emmett-Teller (BET) method, Fourier transform infrared spectroscopy (FTIR), temperature-programmed desorption of NH_3 (NH_3-TPD), temperature-programmed reduction of H_2 (H_2-TPR), and X-ray photoelectron spectroscopy (XPS) in this study.

Experimental

Catalyst preparation

All the catalysts in this study were prepared by impregnation method. The r-Al_2O_3 was first dried at 105 °C for 2 h and then calcined at 300 °C to remove some of the impurities on the surface. After that, $Mn(CH_3COO)_2{\cdot}4H_2O$(Sinopharm Chemical Reagent Co., Ltd., AR), $Ce(NO_3)_3{\cdot}6H_2O$ (Aladdin Industrial Corporation, 99.5%), and $Zr(NO_3)_4{\cdot}5H_2O$ (Shanghai Chemical Reagent Co., Ltd., AR) were dissolved in deionized water and used as precursors. The calcined r-Al_2O_3 was then immersed in the aqueous solution at room temperature for 12 h. After filtration, the solid product was dried at 120 °C and then calcined in air at 600 °C for 4 h. The sample was finally crushed and sieved through 100–120 mesh. A series of catalysts were prepared by varying the concentration of the precursor as described above.

Catalytic performance test

Series of experiments were carried out to study the activities of the catalysts. A schematic diagram of the experimental setup was shown in Fig. 1.

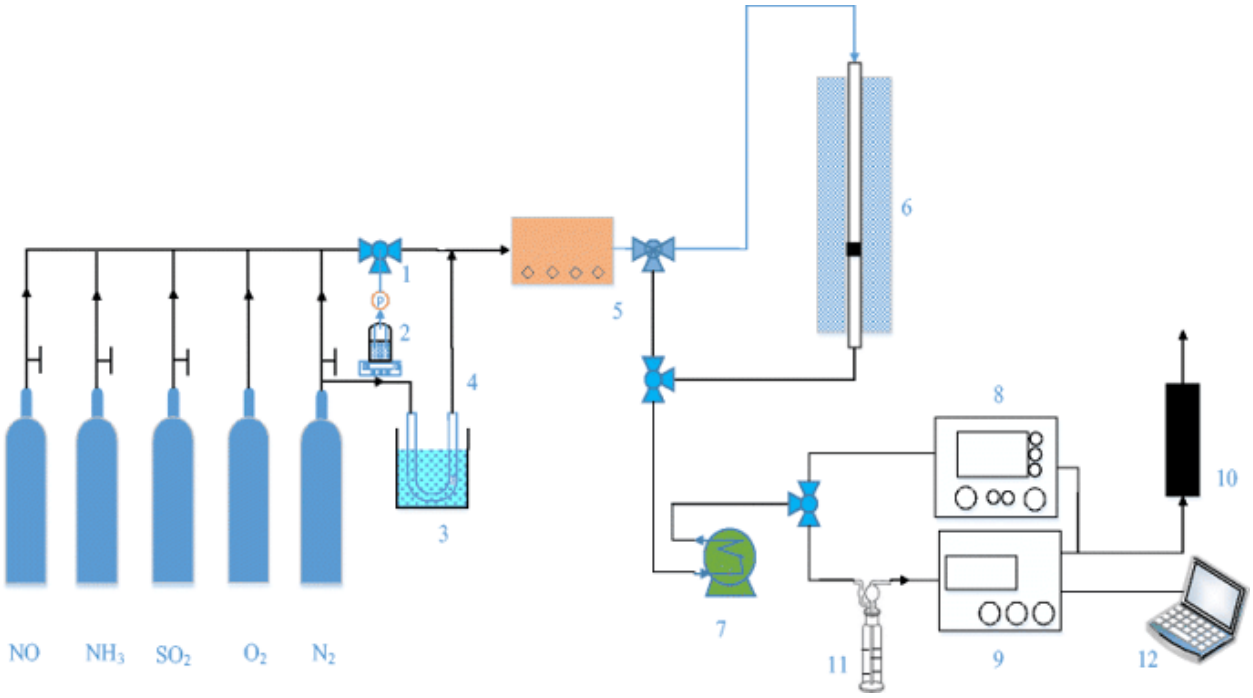

Figure 1. Schematic diagram of the experimental setup. 1 Three-way valve. 2 Water bath. 3 Water bath. 4 Source of mercury. 5 The gas distribution system. 6 Tubular furnace. 7 Condenser. 8 Flue gas analyzer. 9 Hg^0 analyzer. 10 Carbon trap. 11 10% NaOH. 12 Terminal

In this study, the catalyst was placed in a fixed-bed continuous-flow quartz reactor with an inner diameter of 10 mm. The catalytic activity for removing NO_x and Hg^0 was carried out at 100 to 400 °C under 40,000 h^{-1} gas hourly space velocity (GHSV). The simulated flue gas (SFG) was controlled precisely by the mass flow controller, including 1000 ppm NO, 1000 ppm NH_3, 10% O_2, 1000 ppm SO_2 (when used), and N_2 (as a balance). Mercury vapor was produced by a mercury permeation tube (VICI Metronics, Poulsbo, WA, USA), which produced 40.0 μg/m^3 of mercury vapor. Mercury vapor is carried by 300 mL/min pure N_2. When used, 5 vol% H_2O was precisely controlled by a peristaltic pump and injected into the tetrafluoroethylene tubes. H_2O was carried by 200 mL/min pure N_2 and then mixed with SFG. All the tetrafluoroethylene tubes through which Hg^0 and water vapor passed were wrapped in a temperature-controlled heating zone and heated to 60 °C to prevent Hg^0 and water vapor condensation.

The gas was introduced into the reactor at a feed rate of 933 mL/min (volume velocity 40,000 h^{-1}) by the gas distribution system (PQ-07QPP, China). The NO_x and Hg^0 concentrates at the inlet (NO_{xin}/Hg^0_{in}) and the outlet (NO_{xout}/Hg^0_{out}) were measured by a flue gas analyzer (NOVA plus RCU, MRU-Instruments, Neckarsulm-Obereisesheim, GER) and an online measurement instrument (VM-3000, GER). Prior to entering the mercury analyzer, the acid gas and NH_3 were removed by the conditioning unit with 10% NaOH solution. At the same time, water vapor was removed through the condenser. When the reaction temperature reached the preset temperature for 30 min, the reaction reached a steady state, and data were recorded. Hg^0 and NO_x conversions were defined by Eqs. (1) and (2), respectively.

$$\eta_{\mathrm{Hg}}(\%) = \frac{\mathrm{Hg}^0_{\mathrm{in}} - \mathrm{Hg}^0_{\mathrm{out}}}{\mathrm{Hg}^0_{\mathrm{in}}} \times 100\% \quad (1)$$

$$\eta_{\mathrm{NO}\chi}(\%) = \frac{\mathrm{NO}_{\chi\mathrm{in}} - \mathrm{NO}_{\chi\mathrm{out}}}{\mathrm{NO}_{\chi\mathrm{in}}} \times 100\% \quad (2)$$

Characterization

The X-ray diffraction experiments were performed to understand the crystal structure of the catalyst. The XRD pattern of the samples was recorded at room temperature using Cu-Kα radiation ($\lambda = 0.1540$ nm) in a Rigaku D/mas-2500 powder diffractometer (Rigaku, Tokyo, Japan). Data were collected in the range of 10° to 80° scattering angle (2θ) in steps of 0.02° with a detection condition of 40 kV and 200 mA.

The BET surface area, pore volume, and average pore size are very important physical properties in understanding the catalyst, and they were obtained from the N_2 adsorption isotherm using a Micromeritics Tristar II 3020 analyzer (Micromeritics Instrument Corp., Norcross, GA, USA). The BET specific surface area was obtained by multipoint linear fitting, and the pore volume was obtained by the single condensation point method (where $P/P_o = 0.9963$). The pore structure was determined by the adsorption isotherm. Average pore size was calculated using the formula $4V/A$ (where V is the pore volume, and A is the adsorption BET specific surface area).

FTIR spectroscopy was performed using a Shimadzu (Kyoto, Japan) FTIR-8400S IRprestige-21 instrument to study the chemical composition of the catalyst. FTIR spectra were recorded with 20 scans at a spectral resolution of 2 cm^{-1}. The sample powder (2 mg) was mixed with KBr (200 mg, spectrally) and then compressed on a hydraulic press.

The NH_3-TPD was performed on an AutoChem II automatic chemical adsorption device (AutoChem II 2920, Micromeritics) to obtain surface acidity. First, a 200-mg sample was pretreated with airflow (30 mL/min) at 500 °C for 30 min. The samples were then cooled to 100 °C, exposed to NH_3 equilibrium, and rinsed with pure He at the same temperature to avoid adsorption of NH_3. Thereafter, the NH_3-saturated sample was heated to 700 °C in He at a heating rate of 10 °C/min.

The H_2-TPR experiment was carried out to characterize the reduction of the samples using an AutoChem II 2920 (Micromeritics). Prior to analysis, a 50-mg sample was treated at 300 °C for 30 min in a 50-mL/min He stream, and the sample was cooled below 100 °C. Then, the reactor temperature was raised from 100 to 700 °C at a rate of 10 °C/min while the consumption of nitrogen was recorded.

The XPS measurements were performed on an ESCALab250i-XL electron spectrometer (Thermo Fisher VG Scientific, Waltham, MA, USA) using 300 W AlKα S3 radiation to obtain the oxidation state on the surface of the catalyst. The base pressure was about 3×10^{-9} mbar, and the binding energies were referenced to the C1s line at 284.8 eV from adventitious carbon.

Results and discussion

Catalyst performance

Catalyst activity of x% $Ce_{0.2}Zr_{0.3}Mn_{0.5}/r\text{-}Al_2O_3$. The simultaneous removal of NO_x and Hg^0 in the simulated flue gas was investigated at 40,000 h^{-1} GHSV and the results were shown in Fig. 2.

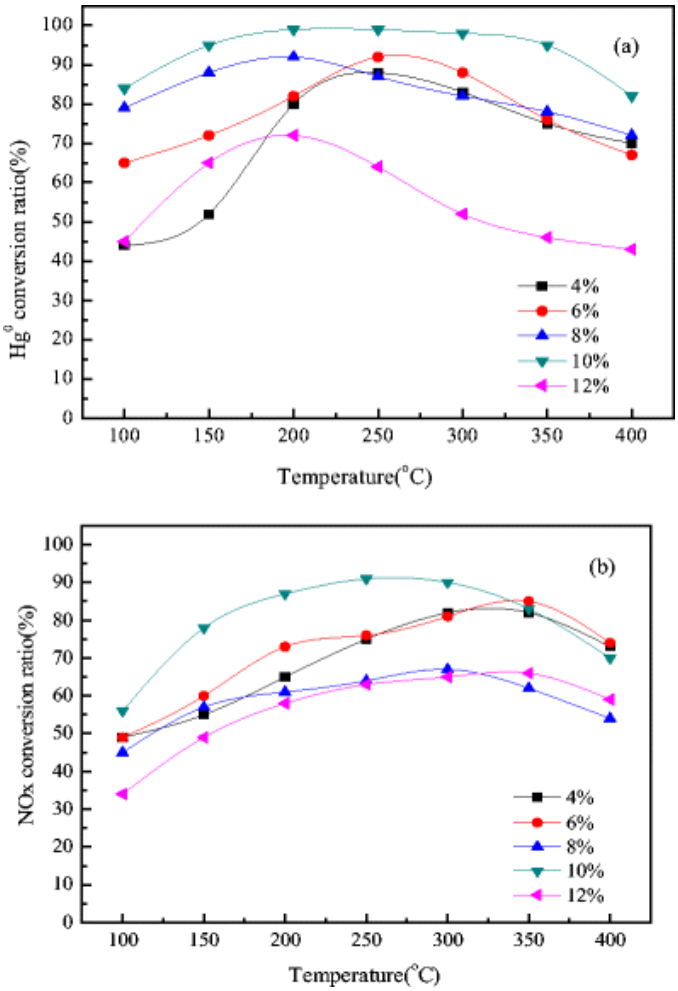

Figure 2. The influence of loaded mass of $Ce_{0.2}Zr_{0.3}Mn_{0.5}O_2$ on co-purification of **a** Hg^0 and **b** NO_x (reaction condition: 42.0 μg/m^3 Hg^0, 1000 ppm NO, NH_3/NO: 1, 10% O_2, GHSV 40,000 h^{-1})

Figure 2 showed that the catalytic activity was significantly affected by the loading active ingredient. With an increase in the loading, the Hg^0 and NO_x conversion ratio first increased and then showed different levels of decline; 10% $Ce_{0.2}Zr_{0.3}Mn_{0.5}O_2/r\text{-}Al_2O_3$ achieved a conversion of Hg^0 and NO_x of up to 97 and 91% at 250 °C, respectively. It was the best catalytic reduction performance of all catalysts tested. The 8% $Ce_{0.2}Zr_{0.3}Mn_{0.5}O_2/r\text{-}Al_2O_3$ has a less denitrification performance of than 6% $Ce_{0.2}Zr_{0.3}Mn_{0.5}O_2/r\text{-}Al_2O_3$ and 10% $Ce_{0.2}Zr_{0.3}Mn_{0.5}O_2/r\text{-}Al_2O_3$. It is probably due to the weaker coordination between metal oxides, making the catalyst less active than the active component dispersed 6% $Ce_{0.2}Zr_{0.3}Mn_{0.5}O_2/r\text{-}Al_2O_3$ (Wang et al. 2017). This indicates that the interaction between metal oxides may be the main reason for the high activity of the catalyst. The BET results showed that the catalyst with a loading of 10% had the largest

BET surface area. It shows that the proper loading of active ingredients helps to provide larger specific surface area and stronger metal oxide interactions. When the loading was increased to 12%, the conversion efficiency appeared to decrease, indicating that the micropores of the catalyst may have become clogged. Optimization of active ingredient loading contributed to the best performance by 10% $Ce_{0.2}Zr_{0.3}Mn_{0.5}O_2$/r-$Al_2O_3$.

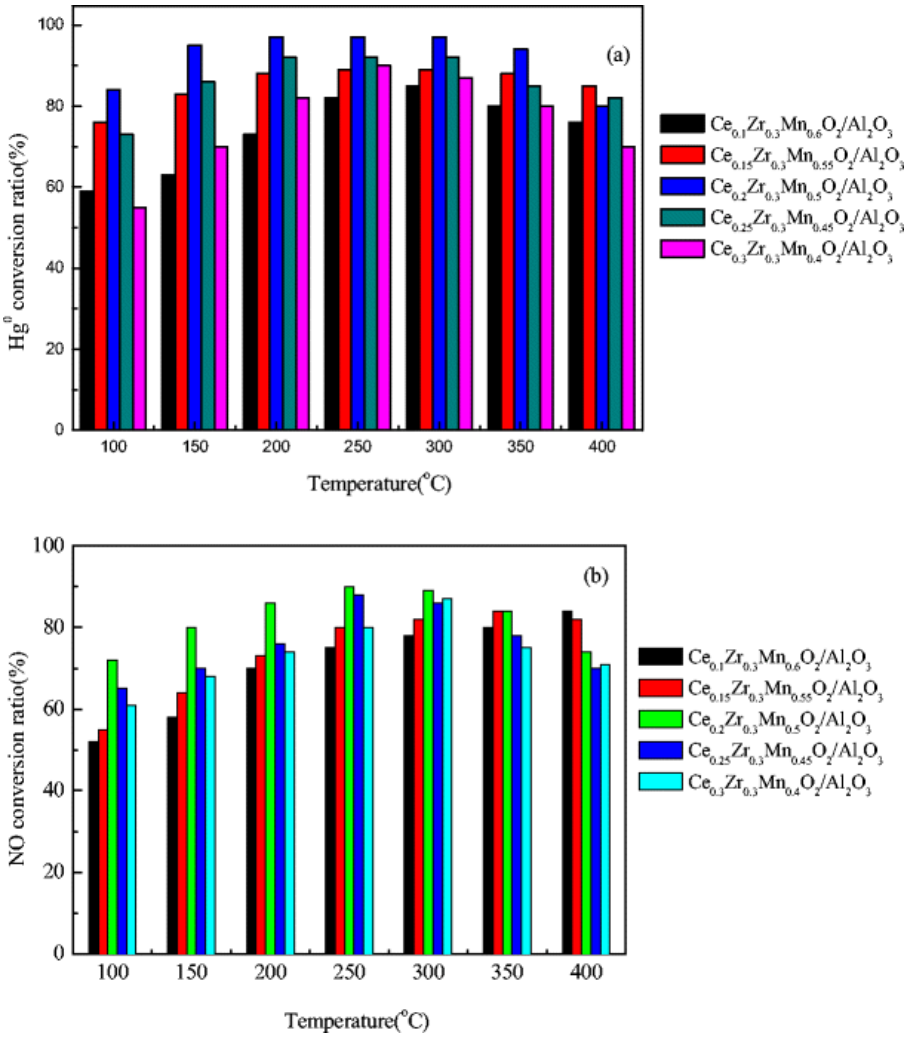

Figure 3. The effect of molar ratio on the simultaneous removal of Hg^0 and NO_x over 10% $Ce_xZr_yMn_zO_2$/r-Al_2O_3: **a** Hg^0 conversion efficiency and **b** NO_x conversion efficiency (reaction conditions: 42.0 μg/m^3 Hg^0, 1000 ppm NO, NH_3/NO: 1, 10 vol% O_2, GHSV 40,000 h^{-1})

Effect of the Ce: Mn molar ratio. In order to further study the influence of the molar ratio of Ce: Mn on the redox properties of the catalysts, a series of catalysts which 10% loaded mass and different molar ratio were prepared. And the performances of NO_x and Hg^0 removal of those catalysts were also explored. The results were shown in Fig. 3.

It was obviously that the conversion of Hg^0 and NO_x were significantly affected by the Ce: Mn molar ratio. With the increase of the molar ratio of Ce: Mn, the conversion of Hg^0 and NO_x increased first and then decreased. The conversion of Hg^0 and NO_x were obtained 97 and 91%, respectively, at 250 °C when the Ce: Mn molar ratio was 0.3: 0.5. It might be due to a more

catalytic synergy between Mn^{4+} species and Ce^{3+} in the catalyst when Ce: Mn molar ratio was 0.3: 0.5, which would be more conducive to the catalytic purification of Hg^0 and NO_x (Yang et al. 2018). Cao et al. (2014) found that the presence of Mn^{4+} significantly promoted the NO_x conversion rate in NH_3-SCR. It had already been reported that the amount of Ce could effectively change the catalyst grain size, which would greatly enhance its reduction ability (Shen et al. 2013). However, when the Ce: Mn molar ratio was further increased and over 0.3:0.5, the performance of the catalysts were obviously decreased. It might due to the lowering of the catalytic synergy of the catalyst, which resulted in the decrease of the oxygen storage capacity and catalytic activity of the catalyst.

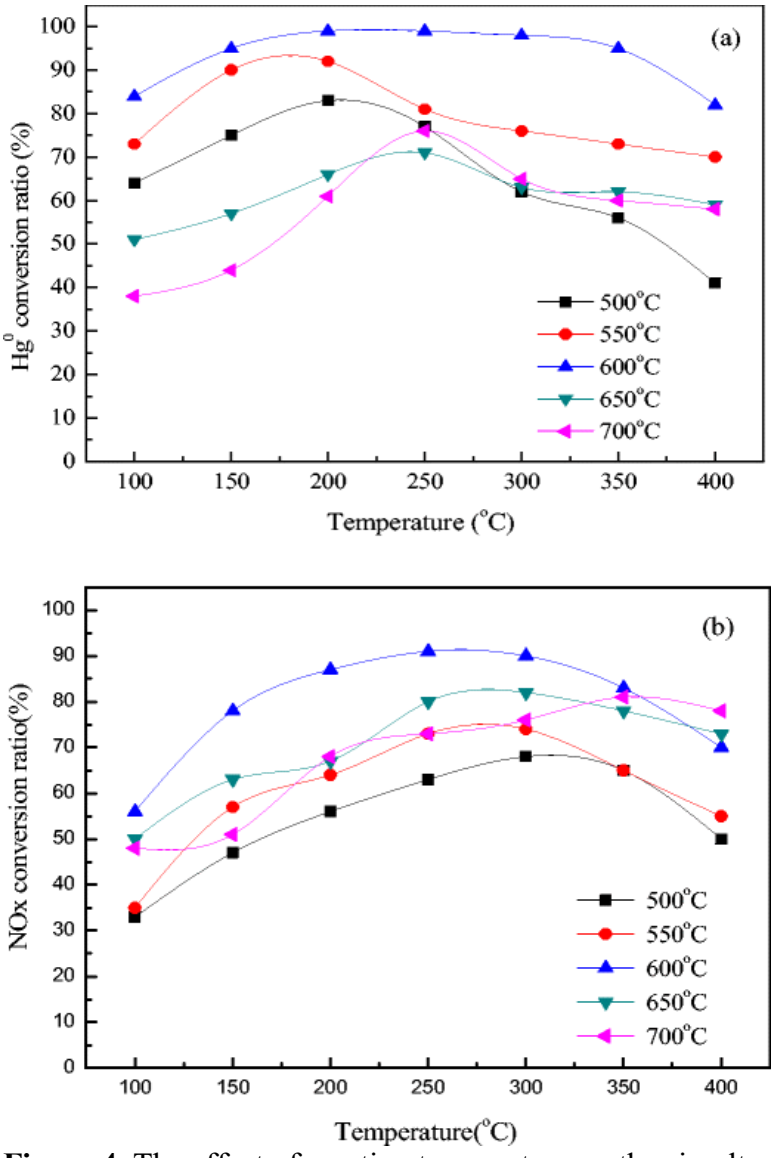

Figure 4. The effect of roasting temperature on the simultaneous removal of Hg^0 and NO_x over 10% $Ce_{0.2}Zr_{0.3}Mn_{0.5}O_2$/r-$Al_2O_3$: **a** Hg^0 conversion efficiency and **b** NO_x conversion efficiency (reaction conditions: 42.0 μg/m^3 Hg0, 1000 ppm NO, NH_3/NO: 1, 10 vol% O_2, GHSV 40,000 h^{-1})

Effect of roasting temperature. When treated at different calcination temperatures, the catalysts have different texture properties, oxygen storage properties, and surface acidities (Wang et al. 2015; Prabhakaran et al. 2017). So, the calcination temperature is one of the key parameters in the preparation of a catalyst. The effect of roasting temperature on the performance of the catalyst was studied by preparing a series of catalysts at different roasting temperatures regarding their activities. The effects of different calcination temperatures on the simultaneous removal NO_x and Hg^0 by 10% $Ce_{0.2}Zr_{0.3}Mn_{0.5}$ were shown in Fig. 4.

Figure 4 showed that as the calcination temperature increased, the conversion of Hg^0 and NO_x first increased and then decreased. In Fig. 4a, b, the catalyst with a calcination temperature of 600 °C had a mercury removal rate of 99% and a NO_x conversion of 90% or more at 250 °C, indicating the best catalytic performance. This might be attributed to the calcination temperature of 600 °C providing optimum texture properties, oxygen storage properties, and surface acidity to the catalyst, which was similar to the results reported by Prabhakaran et al. (2017). When the temperature increased to 650 °C, the activity of the catalyst was decreased. It might be due to the fact that the pore structure of the carrier was sintered or the structure was collapsed when the calcination temperature was too high. It resulted in a decreasing of the active site of the catalyst, which would inevitably lead to the reduction of catalyst activity of 10% $Ce_{0.2}Zr_{0.3}Mn_{0.5}O_2$/r-$Al_2O_3$.

Lifetime of 10% $Ce_{0.2}Zr_{0.3}Mn_{0.5}$/r-Al_2O_3. The stability of a catalyst is closely related to the industrial application of the catalyst, which is usually expressed in terms of lifetime. At 250 °C, the conversion of NO_x and Hg^0 over 10% $Ce_{0.2}Zr_{0.3}Mn_{0.5}$/r-Al_2O_3 was explored over time to examine the lifetime of the catalyst. The results were shown in Fig. 5.

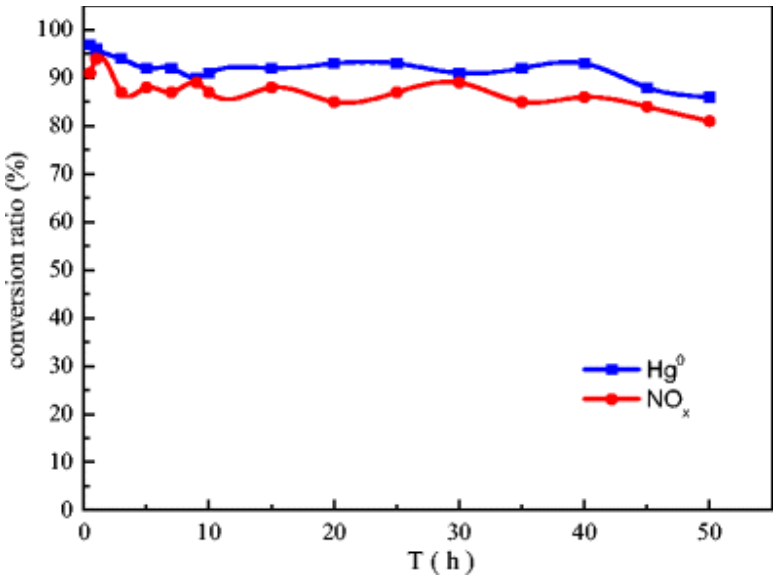

Figure 5. The effect of time on the simultaneous removal of Hg^0 and NO_x over 10%$Ce_{0.2}Zr_{0.3}Mn_{0.5}$/r-Al_2O_3 (reaction conditions: 42.0 μg/m^3 Hg^0, 1000 ppm NO, NH_3/NO: 1, 10 vol% O_2, GHSV 40,000 h^{-1})

Figure 5 showed that the conversion of NO_x increased after 0.5 h, and then appeared to fluctuate slightly, obtaining a retention of 85% after 50 h. The Hg^0 removal efficiency decreased by 12%

during first 10 h and then decreased more slowly, falling by 5% after 40 h. In general, the lifetime of the 10% $Ce_{0.2}Zr_{0.3}Mn_{0.5}$/r-Al_2O_3 catalyst was relatively long, which indicated its good stability.

Effect of H_2O and SO_2 on simultaneous removal of NO_x and Hg^0. H_2O and SO_2 are unavoidable substances in flue gas from bituminous coal plants. Therefore, it is necessary to consider the effects of H_2O and SO_2 on the catalytic performance. This was studied at 250 °C, with 500 ppm SO_2 and 5 vol% H_2O introduced into the airflow, and the results were shown in Fig. 6.

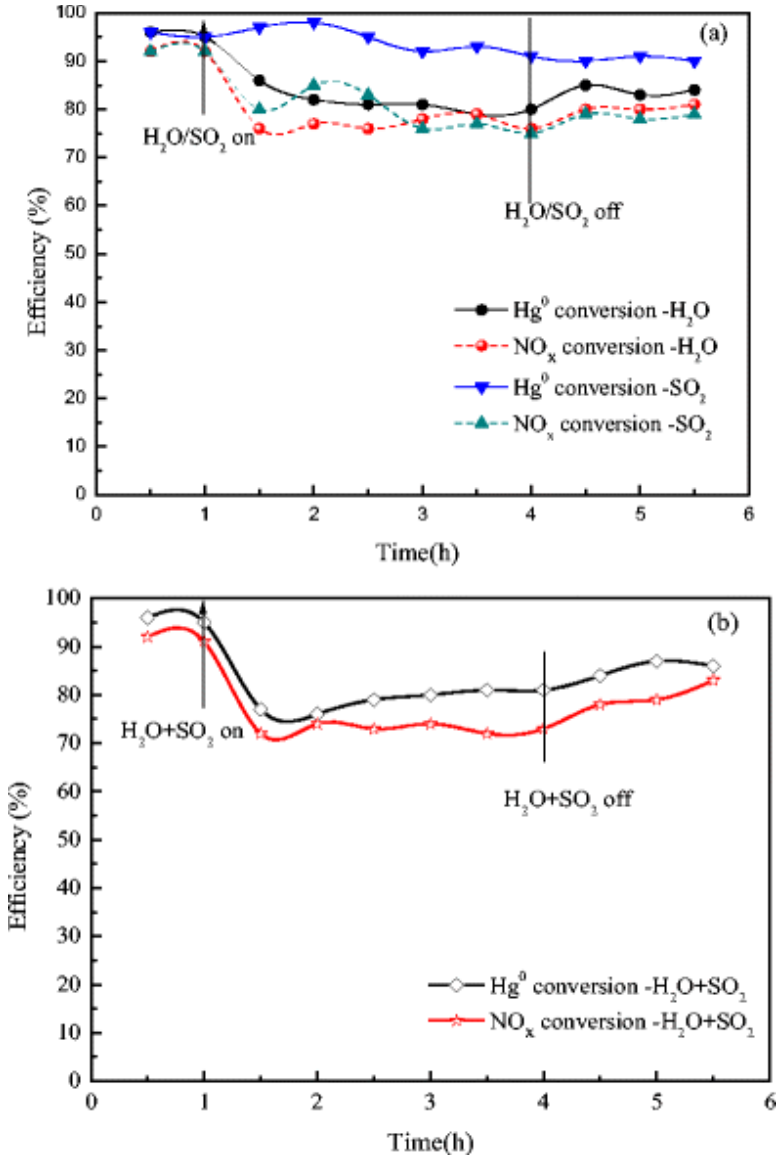

Figure 6. The influence of H_2O and SO_2 on the simultaneous removal of Hg^0 and NO_x over 10%$Ce_{0.2}Zr_{0.3}Mn_{0.5}$/r-Al_2O_3 at 250 °C: **a** the effect of H_2O/SO_2 and **b** the effect of H_2O and SO_2 (reaction conditions: 42.0 μg/m^3 Hg^0, 1000 ppm NO, NH_3/NO: 1, 10% O_2, 10 vol% H_2O (when used), 500 ppm SO_2 (when used), GHSV 40,000 h^{-1})

Figure 6a showed that when 5 vol% H_2O was introduced, the conversion rate of NO_x and Hg^0 decreased, indicating that H_2O competes for active sites, which was similar to the report by Li Y et al. (2008). However, the conversion rate of NO_x and Hg^0 still remained at 84 and 87% after introducing H_2O for 2 h, respectively, showing its acceptable water resistance.

When 500 ppm SO_2 was introduced, the mercury conversion rate first slightly increased and then decreased to a certain extent. The increase in mercury conversion rate indicated that SO_2 could promote the oxidation of Hg^0, which was also found in the studies by Wan et al. (2011) and Zhao et al. (2016a). By accommodating more surface lattice oxygen species, CeO_2 could catalyze SO_2 oxidation to produce SO_3 and then react with Hg^0 to form $HgSO_4$ on the CeO_2 surface (Gu et al. 2010; Yang et al. 2017b). However, continued SO_2 would react with gas-phase oxygen to produce SO_3, which in return inhibited the mercury oxidation due to the synthetic competing effect (Fan et al. 2010; Qi et al. 2004). Correspondingly, compared with the mercury removal efficiency, the NO_x removal efficiency decreased slightly. SO_2 inhibited the formation of key intermediates of nitrate (Zhou et al. 2016b; Xu et al., 2009). It was possible that SO_2 reacted with NH_3 on the catalyst surface to produce ammonia or bisulfate and other substances deposited on the catalyst surface, which broke the connection between the active sites and NH_3, thereby reducing the conversion rate of NO_x and Hg^0 (Xu et al. 2009).

Figure 6b showed the effect of simultaneous introduction of H_2O and SO_2. The conversion rates of NO_x and Hg^0 were reduced to 78 and 81%, respectively. When the introduction of H_2O and SO_2 ceased, the conversion rates of NO_x and Hg^0 reverted to 84 and 85%, respectively, but not to the original level, possibly because the damage caused by ammonium sulfate and other substances at the catalyst's active sites was not fully restored (Zhao et al. 2016a; Qi et al. 2004; Qi and Yang 2003). In the main reaction period, the activity of 10% $Ce_{0.2}Zr_{0.3}Mn_{0.5}O_2$/r-$Al_2O_3$ was still maintained at a very high level, which indicated that the catalyst was reasonably resistant to water and sulfur.

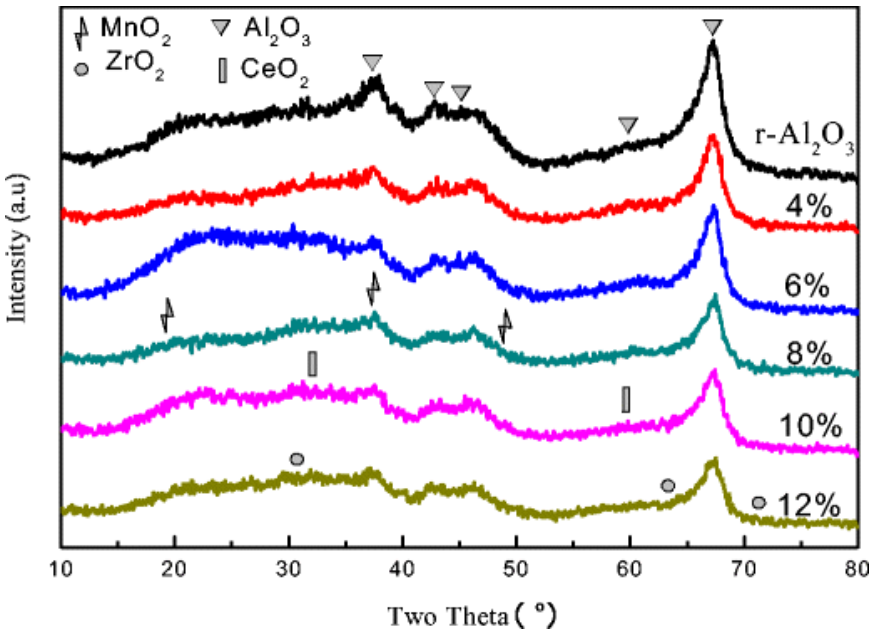

Figure 7. XRD patterns of $Ce_{0.2}Zr_{0.3}Mn_{0.5}O_2$/r-$Al_2O_3$ and r-Al_2O_3

Catalyst characterization

XRD. The XRD experiments were carried out to understand the crystal structure of *x*% $Ce_{0.2}Zr_{0.3}Mn_{0.5}O_2$/r-$Al_2O_3$ (4, 6, 8, 10, and 12%) and r-Al_2O_3, and the results were shown in Fig. 7.

Several diffraction peaks observed at 37.09°, 42.54°, 45.84°, 60.42°, and 67.00° matched the support r-Al_2O_3 very well (PDF#04-0875). While, the appearance of the peaks at 33.29° and 60.00° could be due to the cubic CeO_2 crystallite (PDF#34-0394). The appearance of the peaks at 19.29°, 37.5°, and 49.2° could be due to the cubic MnO_2 crystallite (PDF#34-0394) and the appearance of the peaks at 30.4°, 62.8°, and 74.5° could be due to the cubic ZrO_2 crystallite (PDF#02-0733) (Leitenbur et al. 1996; Liu et al. 2014; Qi and Yang 2003). When the loading is less than 6%, peaks of CeO_2, ZrO_2, and MnO_2 are not observed in Fig. 7. It could be inferred that Ce, Zr, and Mn species were amorphous or highly dispersed in the catalyst. When the loading is more than 6%, the weak peaks of CeO_2, ZrO_2, and MnO_2 appear, which indicates that CeO_2, ZrO_2, and MnO_2 crystallites are formed on the catalyst. Especially when the loading is 10%, a new r-Al_2O_3 peak appears at 39.62°, suggesting that there may be interactions between metal oxides. For example, the formation of CeO_2, ZrO_2, and MnO_2 crystallites leads to the transfer of r-Al_2O_3 peak. These interactions may be the reason for the highest catalytic activity of 10% $Ce_{0.2}Zr_{0.3}Mn_{0.5}O_2$/r-$Al_2O_3$ catalyst. With an increase of the loading, the half-width of the *x*% $Ce_{0.2}Zr_{0.3}Mn_{0.5}O_2$/r-$Al_2O_3$ catalyst at 67.0° widened, and the peak intensity decreased, which indicated that the effect of the loading of the active component $Ce_{0.2}Zr_{0.3}Mn_{0.5}O_2$ on the catalyst structure reduced the crystal size. It had been reported that amorphous microcrystalline materials with large structural distortions would provide more catalytic reactive sites than crystalline materials, leading to higher catalytic activity (Zhao et al. 2016b).

BET. The BET surface area, pore volume, and average pore size were summarized in Table 1 for different samples.

Table 1. Surface structure properties of $Ce_{0.2}Zr_{0.3}Mn_{0.5}O_2$/r-$Al_2O_3$ catalysts

Catalyst	Surface area (m^2/g)	Pore volume (cm^3/g)	Pore size (nm)
r-Al_2O_3	214.22	0.445	17.32
4%	46.08	0.312	23.52
6%	48.94	0.511	35.55
8%	63.03	0.467	25.92
10%	84.13	0.533	21.39
12%	57.65	0.528	31.55

From Table 1, it could be found that when the metal oxides were loaded onto γ-Al_2O_3, the surface areas of the samples were decreased significantly. However, when the load was further increased, the physical properties of the catalyst were reduced to some extent. In particular, the catalyst with a loading of 10% showed the maximum specific surface area, which was consistent with the catalytic performance. A higher BET specific surface area might provide more active sites, thereby promoting catalytic activity. However, with the further increased in the amount of loading, the active component sintered on the carrier, resulting in a decrease in the physical properties of the catalyst.

FTIR. The chemical composition of a catalyst is very important to study the mechanism of catalytic reaction. Therefore, FTIR characterization of 4, 6, 8, 10, and 12% $Ce_{0.2}Zr_{0.3}Mn_{0.5}O_2$/r-$Al_2O_3$ and r-Al_2O_3 were carried out, and the results were shown in Fig. 8.

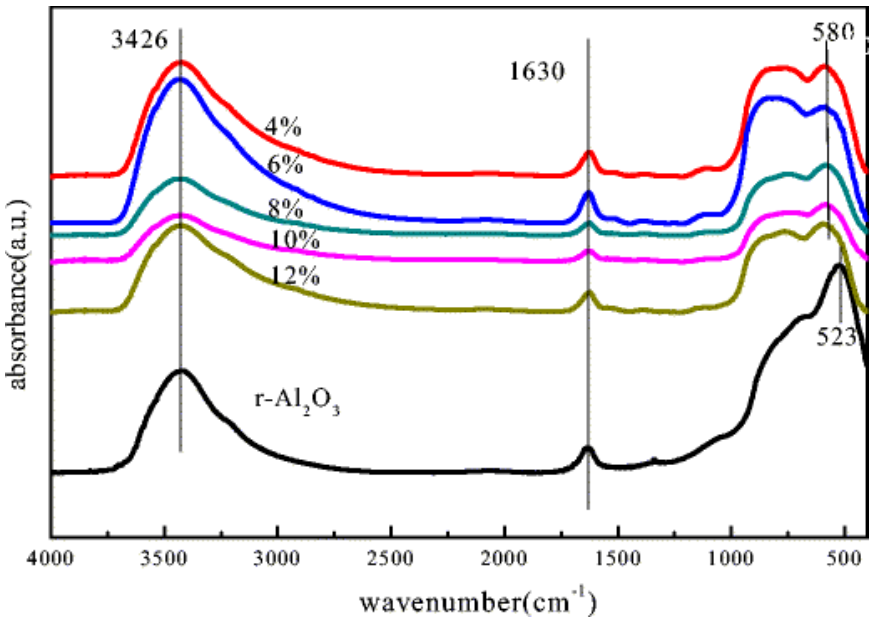

Figure 8. FT-IR analysis of the catalysts

The same wavenumber bands appeared at 3445 and 1639 cm^{-1}, but there were differences in the number of wavenumber bands below 1000 cm^{-1}. The strong absorption peak at 3445 cm^{-1} was the vibration absorption peak of the hydroxyl group contained on the surface of the catalyst pore. The weak peak at 1639 cm^{-1} was the OH^- bending vibration peak in the crystal water (Terribilea et al. 1998). The obvious peak at 580 cm^{-1} belonged to the telescopic vibration effect of Mn-O and Al-O, since Mn–O vibration was the major factor that resulted from manganese accounting for the largest proportion of the catalyst (Ludvigsson et al. 2001; Buciuman et al. 1999). The smaller peaks at 700 and 792 cm^{-1} might be related to the bending of Ce-O, and Ce-Zr-O, which interacted with the vector (Li et al. 2006). While the peaks at 530 cm^{-1} might be related to the bending of Al-O, which was consistent with the report of J. Li et al. (Buciuman et al. 1999). The peaks formed by the different supported catalysts were the same, indicating that the active component formed the same material on the catalyst support.

NH_3-TPD. The surface acid properties of the catalysts were analyzed by NH_3-TPD. The results were shown in Fig. 9.

Two main ammonia desorption peaks were observed over the entire desorption temperature range in Fig. 9, located at 170–190 and 390–410 °C. According to the literatures (Ma et al. 2015; Lee et al. 2013; Xu et al. 2012), the peak at 170–190 °C should be attributed to the NH_3 decomposition from the strong Brønsted acid sites, the peak at 390–410 °C was attributed to desorption of coordinated NH_3 bound to the Lewis acid sites. In addition, when the loading was 10%, a slight NH_3 desorption peak appeared at a high temperature of 485 °C, indicating that a new strong acidic center was formed and resulted in a loading of 10% showing higher catalytic

performance. Lietti et al. (1996) and Xie et al. (2004) pointed out that the strong acid in the catalyst played an important role in improving the low-temperature activity of the catalyst.

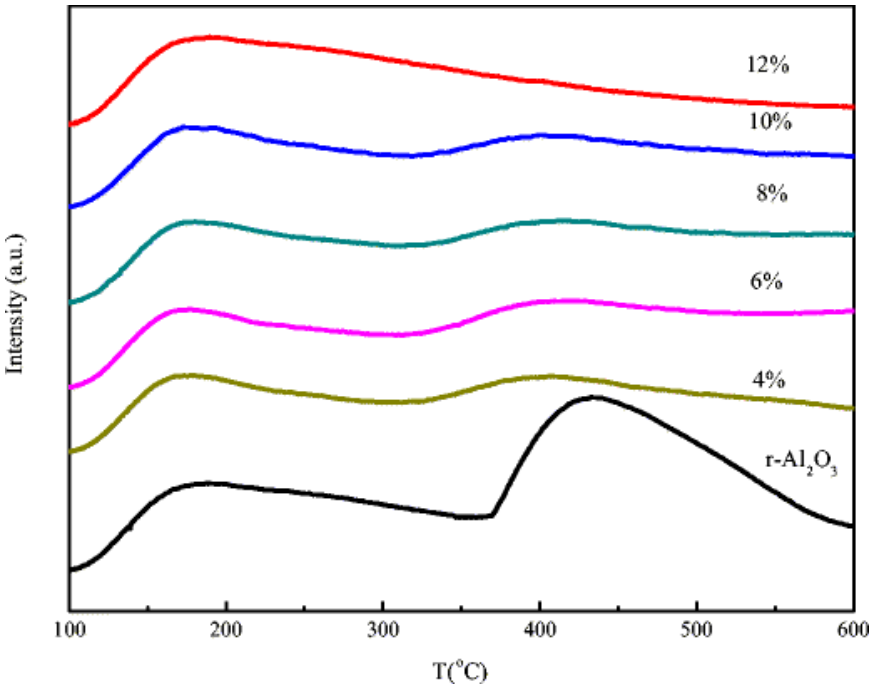

Figure 9. NH_3-TPD analysis of the catalysts

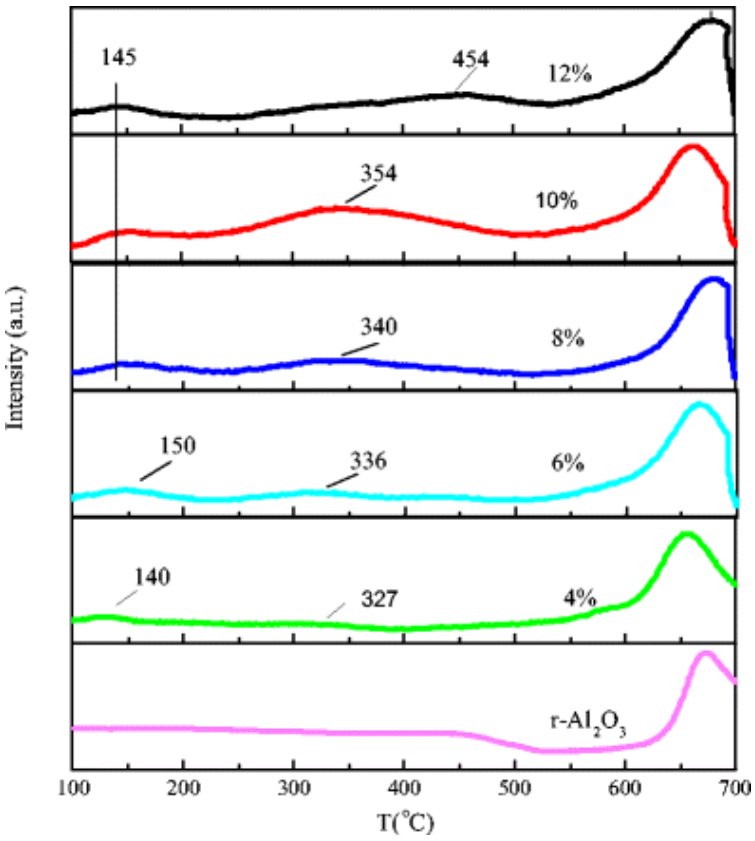

Figure 10. H_2-TPR analysis of the catalysts

The 12% loading of the catalyst also showed good low-temperature activity. However, its NH_3 desorption peak intensity was not obvious at 390–410 °C, indicating that there were no abundant acid sites on its surface. Coupled with the XRD and BET results, the excessive loading of $Ce_{0.2}Zr_{0.3}Mn_{0.5}O_2$ on the substrate led to a decrease of the specific surface area and then a reduction of the active sites of NH_3 adsorption, thus inhibiting its catalytic activity. Therefore, the appropriate loading of $Ce_{0.2}Zr_{0.3}Mn_{0.5}O_2$ in the catalyst would improve the catalytic performance, especially at low temperature.

H_2-TPR. The redox properties of 4, 6, 8, 10, and 12% $Ce_{0.2}Zr_{0.3}Mn_{0.5}O_2$/r-$Al_2O_3$ and r-Al_2O_3 were studied by the H_2-TPR technique to obtain the reduction features of the sample as shown in Fig. 10.

Figure 10 showed that there were three main absorption peaks at about 140–150, 300–350, and 650–700 °C, respectively. The pure Al_2O_3 surface reduction reaction was given as Eq. (3). The third peak at 650–700 °C was attributed to the reduction of Al_2O_3. Ettireddy et al. (2007), Shen et al. (2014), and Trawczyński et al. (2005) demonstrated that MnO_x was reduced by H_2 in the following order: $MnO_2 \rightarrow Mn_2O_3 \rightarrow Mn_3O_4 \rightarrow MnO$. According to XPS characterization results, the reduction peak at 150 °C could be attributed to the reduction of highly dispersed MnO_2 that has a strong interaction with CeO_2, ZrO_2, or carriers (Trawczyński et al. 2005). The reduction peak at 300–350 °C was formed by the reduction of Mn_2O_3 to MnO and surface Ce^{4+} to Ce^{3+} (Qu et al. 2014; Tang et al. 2008; Su et al. 2013). Especially in the 10% $Ce_{0.2}Zr_{0.3}Mn_{0.5}O_2$/r-$Al_2O_3$, the peak was much more obvious, indicating that the 10% $Ce_{0.2}Zr_{0.3}Mn_{0.5}O_2$/r-$Al_2O_3$ catalyst contained more high-valence manganese and cerium species, which could highly support the strong synergetic effect on the mobility of surface oxygen and the activation of lattice oxygen (Tang et al. 2006, 2008). The weak wave peak at 550–600 °C was attributed to the reduction of chemisorbed oxygen (Lian et al. 2014). It was consistent with the results and discussion of Fig. 3.

$$Al_2O_3 + 3H_2 \rightarrow 2Al + 3H_2O \quad (3)$$

Combined with the results of the simultaneous removal of NO and Hg^0, the catalysts had high catalytic efficiency at low temperature, mainly because of the reduction of Mn^{4+} to Mn^{3+} at low temperature, supporting that low oxygen vacancy formation energy of MnO_2 provided a favorable thermodynamic pathway for the catalytic reoxidation by gas-phase oxygen. Meanwhile, because of the strong synergistic effect of Mn, Ce, and Zr species, the higher redox capacity of 10% $Ce_{0.2}Zr_{0.3}Mn_{0.5}O_2$/r-$Al_2O_3$ could enhance the mobility of surface oxygen (Tang et al. 2006). Synergistic effects were believed to lead to severe structural deformations and oxygen-enriched defects (Xu et al. 2014, 2015), which could improve its catalytic performance.

XPS. The surface chemical states of Ce, Zr, Mn, and O in fresh 10% $Ce_{0.2}Zr_{0.3}Mn_{0.5}O_2$/r-$Al_2O_3$ and used 10% $Ce_{0.2}Zr_{0.3}Mn_{0.5}O_2$/r-$Al_2O_3$ were determined by XPS analysis to understand the mechanism of NO_x and Hg^0 removal, and the results were shown in Fig. 11.

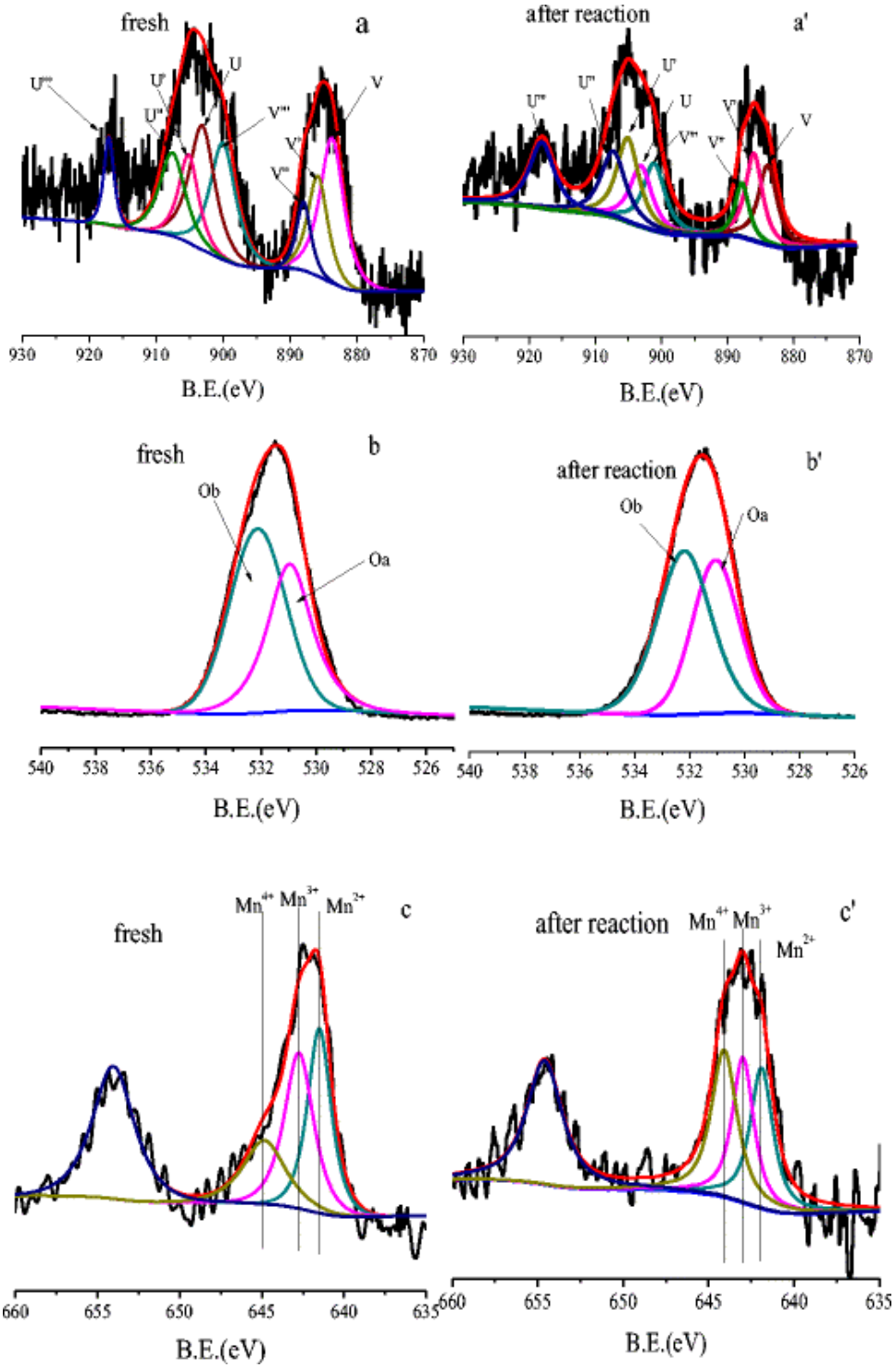

Figure 11. a–**c** XPS spectra of Ce, Zr, Mn, O of fresh 10% $Ce_{0.2}Zr_{0.3}Mn_{0.5}O_2$/r-$Al_2O_3$ and after the reaction of 10% $Ce_{0.2}Zr_{0.3}Mn_{0.5}O_2$/r-$Al_2O_3$

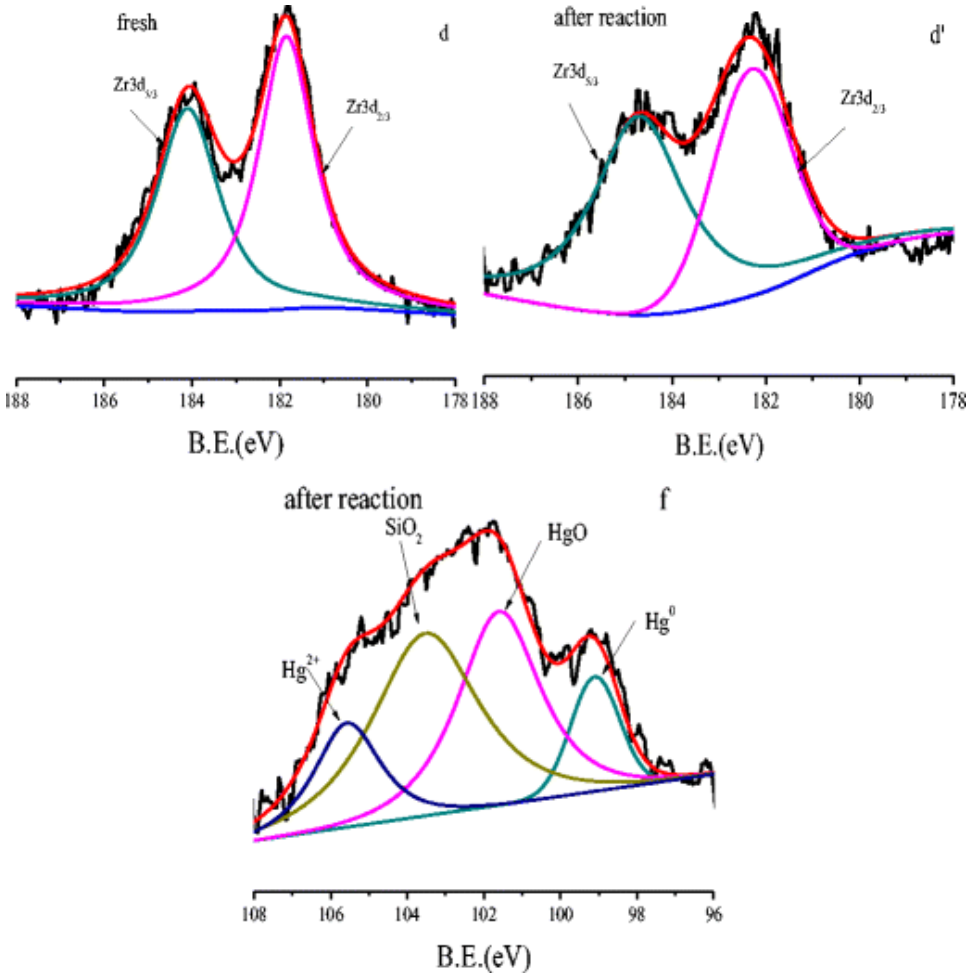

Figure 11 (continued). a–c XPS spectra of Ce, Zr, Mn, O of fresh 10% $Ce_{0.2}Zr_{0.3}Mn_{0.5}O_2$/r-$Al_2O_3$ and after the reaction of 10% $Ce_{0.2}Zr_{0.3}Mn_{0.5}O_2$/r-$Al_2O_3$

Ce3d spectra could be fitted into eight peaks, labeled u, u′, u″, u‴, v, v′, v″, v‴, which could be attributed to four pairs of 3d5/2 and 3d3/2 bimodal spin orbitals. The u, u″, u‴, v, v″, and v‴ peaks were Ce^{4+}, and the peaks denoted as u′ and v′ were Ce^{3+} (Mullins et al. 1998). From Fig. 11, there was a large amount Ce^{4+} in the 10% $Ce_{0.2}Zr_{0.3}Mn_{0.5}O_2$/r-$Al_2O_3$ catalyst, while the Ce^{3+} amount was limited. The presence of Ce^{3+} could lead to a charge imbalance (Li et al. 2011). Because of the presence of Ce^{3+}, it was easy to produce oxygen vacancies that were conducive to the formation of surface chemisorbed oxygen (Li et al. 2011, 2012). Therefore, some Ce^{3+} ions associated with the oxygen species adsorbed on the surface of the catalyst could improve the oxidation efficiency of Hg^0. In Fig. 11(a′), after the reaction, the proportion of Ce^{4+}/Ce^{3+} of used 10% $Ce_{0.2}Zr_{0.3}Mn_{0.5}O_2$/r-$Al_2O_3$ decreased slightly, indicating that some Ce^{4+} had undergone reduction.

The O1s peak could be fitted to two characteristic peaks: 530.3 and 531.9 eV, which were attributed to lattice oxygen (denoted as Oa) and chemisorbed oxygen (expressed as Ob) (Chang et al. 2015), respectively. In Fig. 11b, the Ob/(Oa + Ob) ratio was very large, suggesting that the chemisorbed oxygen was significantly higher than lattice oxygen. Since chemisorbed oxygen was the most active oxygen regarding the oxidation reaction, 10% $Ce_{0.2}Zr_{0.3}Mn_{0.5}O_2$/r-$Al_2O_3$

showed excellent Hg^0 oxidation activity (Madier et al. 1999). In Fig. 11(b′), the chemisorbed oxygen decreased after the reaction, indicating that some chemisorbed oxygen was converted, which was consistent with the result of TPR in Fig. 10.

For the Mn2p XPS spectrum, two main signals of the binding energy due to Mn2p3/2 (at 636 eV) and Mn2p1/2 (at 660 eV) could be observed in Fig. 11c (He et al. 2014). Using a peak-fitting deconvolution, the Mn 2p3/2 spectra could be separated into three characteristic peaks: 641.5–641.7, 642.7–642.9, and 644.3–644.6 eV, assigned to Mn^{2+}, Mn^{3+}, and Mn^{4+}, respectively. Binding energies of Mn 2p3/2 in the 10% $Ce_{0.2}Zr_{0.3}Mn_{0.5}O_2$/r-$Al_2O_3$ catalyst measured here (640–645 eV) were slightly higher than those of MnO, Mn_2O_3, and MnO_2 reported elsewhere, which showed a nice distinction in the change in chemical environment between the CeO_2, ZrO_2, and MnO_x alone, and which also fits well with the results of TPR discussed in Fig. 10 (Zhou et al. 2016a; Shimizu 1992). After the reaction, the binding energy of Mn^{2+} and Mn^{3+} increased, while the binding energy of Mn^{4+} decreased slightly, indicated that some Mn^{4+} was converted to Mn^{2+} and Mn^{3+}. The shift among Mn^{4+}, Mn^{3+}, and Mn^{2+} was beneficial for the generation of labile oxygen vacancies and bulk oxygen species, which was the main reason for the good activity at low temperature of the 10% $Ce_{0.2}Zr_{0.3}Mn_{0.5}O_2$/r-$Al_2O_3$ catalyst (Kim et al. 2009).

The Zr3d XPS spectrum was shown in Fig. 11(d). The peaks of the binding energy at 181.4–182.0 eV were attributed to Zr3d5/2, and the binding energy at 184.0–184.2 eV was ascribed to Zr3d3/2. All bands belonged to Zr^{4+} (Hutson et al. 2007). These results were consistent with studies by D. Jampaiah et al. (2016) and X. Wang et al. (2007), and zirconium had a negligible effect on Hg^0 oxidation by the catalyst. As mentioned above, the addition of Mn and Ce in r-Al_2O_3 could lead to more surface oxygen, especially chemisorbed oxygen, which could promote the removal of NO_x and Hg^0.

The Hg4f XPS pattern was shown in Fig. 11f. The peak at 99.2 eV was attributed to Hg^0 (Xie et al. 2012). The peaks at 101.5 and 105.4 eV corresponded to Hg4f7/2 and Hg4f5/2, respectively, and were assigned to HgO (Yang et al. 2011). The peak at 103.5 eV was attributed to Si2p of SiO_2 in quartz wool (Yang et al. 2011). This indicated that the main species of mercury on the surface of $Ce_{0.2}Zr_{0.3}Mn_{0.5}O_2$/r-$Al_2O_3$ was HgO after the catalytic reaction. Hg^0 was adsorbed on the surface of the $Ce_{0.2}Zr_{0.3}Mn_{0.5}O_2$/r-$Al_2O_3$ catalyst, and then Hg^0 was continuously converted to HgO by the reactive surface oxygen (Lee and Bae 2009). Therefore, Hg^0 oxidation by $Ce_{0.2}Zr_{0.3}Mn_{0.5}O_2$/r-$Al_2O_3$ catalysts might be attributed to the Mars-Maessen mechanism.

Mechanism discussion

From the above studies, the reaction on the 10% $Ce_{0.2}Zr_{0.3}Mn_{0.5}O_2$/r-$Al_2O_3$ catalyst surface included Hg^0 oxidation and NO conversion, which were aided by the synergetic effect on the mobility of chemisorbed oxygen and the activation of lattice oxygen. Based on XPS characterization results, the oxidation of Hg^0 on the surface of 10% $Ce_{0.2}Zr_{0.3}Mn_{0.5}O_2$/r-$Al_2O_3$ was considered to follow the Mars-Maessen mechanism. The gaseous Hg^0 was first adsorbed on the surface of the catalyst by physical adsorption to form Hg(ad) in the adsorbed state and then reacted with Mn_xO_y or Ce_xO_y at the active sites of 10% $Ce_{0.2}Zr_{0.3}Mn_{0.5}O_2$/r-$Al_2O_3$. MnO_2 and CeO_2 provided lattice oxygen to oxidize Hg(ad) and then converted the reduced Mn_2O_3 and

Ce_2O_3 back to the original state by oxygen in the gas. The following reactions were the suggested mechanisms:

$$Hg^0(g) \rightarrow Hg^0(ad) \quad (4)$$

$$2MnO_2 \rightarrow Mn_2O_3 + Oa \quad (5)$$

$$Mn_2O_3 \rightarrow 2MnO + Oa \quad (6)$$

$$2CeO_2 \rightarrow Ce_2O_3 + Oa \quad (7)$$

$$Hg^0(ad) + Oa \rightarrow HgO(ad) \quad (8)$$

$$Mn_2O_3 + 1/2\,O_2(g) \rightarrow 2MnO_2 \quad (9)$$

$$2MnO + 1/2\,O_2(g) \rightarrow Mn_2O_3 \quad (10)$$

$$Ce_2O_3 + 1/2\,O_2(g) \rightarrow 2CeO_2 \quad (11)$$

$$2MnO + 2CeO_2 \rightarrow Mn_2O_3 + Ce_2O_3 \quad (12)$$

$$Mn_2O_3 + 2CeO_2 \rightarrow 2MnO_2 + Ce_2O_3 \quad (13)$$

Hg^0 was adsorbed on surface of the 10% $Ce_{0.2}Zr_{0.3}Mn_{0.5}O_2$/r-$Al_2O_3$ and formed Hg^0 (ad), which could be confirmed from the Hg4f XPS pattern in Fig. 11f, shown as reaction (4). The valence state transition of Mn and Ce produced lattice oxygen (Shimizu 1992) (Reactions (5)–(7)). Reaction (8) showed that Hg^0 (ad) was oxidized by the lattice oxygen to generate HgO. The lower-valence Mn oxides was oxidized to higher-valence ones by gas-phase O_2 as shown in reactions (9)–(10)). Reactions (11)–(13) illustrated that the oxidation-reduction cycle of Ce^{4+}/Ce^{3+} could occur on surface of 10% $Ce_{0.2}Zr_{0.3}Mn_{0.5}O_2$/r-$Al_2O_3$ during the adsorption of mercury, which was shown as the Ce3d XPS pattern in Fig. 11(a'). The consumed lattice oxygen was supplied by the fixed gas-phase O_2 and parts of deactivating oxidization-active sites were recovered, which improved the Hg^0 removal performance of 10% $Ce_{0.2}Zr_{0.3}Mn_{0.5}O_2$/r-$Al_2O_3$.

In addition, based on the results of TPD characterization, Lewis and Bronsted acid sites were observed on the surface of 10% $Ce_{0.2}Zr_{0.3}Mn_{0.5}O_2$/r-$Al_2O_3$ composite catalyst, which might lead to the appearance of NH_3, NH_4^+, and other intermediates. Furthermore, based on the characterization of TPR and XPS, it was known that there was lattice oxygen in the catalyst, which oxidized NH_3 to NH_2^- (Zhao et al. 2016a, b). The mechanism of NH_3-SCR of NO was suggested as follows:

$$NH_3(g) \leftrightarrow NH_3(ad)/NH_4^+ \quad (14)$$

$$O_2(g) \rightarrow O^*(ad) \quad (15)$$

$$2NH_3(g) + [O] \rightarrow 2NH_2(ad) + H_2O \quad (16)$$

$$NO(g) \rightarrow NO(ad) \quad (17)$$

$$NO(ad) + NH_2^-(ad) \rightarrow N_2(g) + H_2O(g) \quad (18)$$

$$2NO(g) + O_2(g) \rightarrow 2NO_2(ad) \quad (19)$$

$$2NH_3(ad) + NO_2(ad) + NO(g) \rightarrow 2N_2 + 3H_2O \quad (20)$$

$$2NH_4^+(ad) + NO_2(ad) + NO(g) \rightarrow 2N_2 + 3H_2O + 2H^+ \quad (21)$$

In the reaction of NO by NH_3-SCR, the gaseous ammonia was firstly absorbed on the acid sites (i.e., Brønsted acid sites and Lewis acid sites) and then formed into absorbed ammonia species (NH_3, NH_4^+), which was very strong compared to the adsorption of NO + O_2 and its products, shown as reaction (14). The gaseous O_2 was adsorpted to form O^* (ad), which can be confirmed by O1s XPS pattern, shown as reaction (15). The absorbed ammonia species was activated by the lattice oxygen to form the amide species on the surface (NH_2^-), shown as reaction (16). The gaseous NO was absorbed (reaction (17)). Then, gaseous NO was reduced by NH_2^- on the surface to form N_2 and H_2O, shown as reaction (18). Meanwhile some of the unabsorbed NO was oxidized to NO_2 by gaseous O_2, which was then reduced to N_2 and H_2O by ammonia (reactions (19)–(21)).

Conclusion

Series of $Ce_xZr_yMn_zO_2$/r-Al_2O_3 catalysts were synthesized for co-purifying of NO_x and Hg^0 from simulated flue gas; 10% $Ce_{0.2}Zr_{0.3}Mn_{0.5}O_2$/r-$Al_2O_3$ exhibited excellent NO_x conversion (91%) and Hg^0 oxidation efficiency (95%) in the SCR atmosphere at 250 °C. Meanwhile, 10% $Ce_{0.2}Zr_{0.3}Mn_{0.5}O_2$/r-$Al_2O_3$ showed a relatively long lifetime, exhibiting good stability, and good resistance to SO_2 and H_2O, which was due to its advantages of low crystallinity, better texture performance, and strong redox ability. According to the TPD, TPR, and XPS characterizations and the catalytic performance of 10% $Ce_{0.2}Zr_{0.3}Mn_{0.5}O_2$/r-$Al_2O_3$, there were the strong acid and high-valence Mn and Ce species in 10% $Ce_{0.2}Zr_{0.3}Mn_{0.5}O_2$/r-$Al_2O_3$, which could effectively promote the removal of NO_x and Hg^0. Therefore, the catalytic mechanisms of the simultaneous removal of NO_x and Hg^0 by 10% $Ce_{0.2}Zr_{0.3}Mn_{0.5}O_2$/r-$Al_2O_3$ were suggested as the reactions of $2NH_3/NH_4^+$ (ad) + NO_2(ad) + NO(g) → 2 N_2 + $3H_2O/2H^+$ and Hg(ad) + [O] → HgO (ad).

Funding

This work was supported by the National Key R&D Program of China (No. 2017YFC0210303), Joint Funds of the National Natural Science Foundation of China (No. U1560110), Beijing Science and Technology Project (No. D161100004516001), and Fundamental Research Funds for the Central Universities.

Author notes

Pei Lu and Huifang Yue contributed equally to this work.

References

Benson SA, Laumb JD, Crocker CR, Pavlish JH (2005) SCR catalyst performance in flue gases derived from subbituminous and lignite coals. Fuel Process Technol 86:577–613 Article CAS Google Scholar

Buciuman F, Patcas F, Craciun R, Zahn D (1999) Chem inform abstract: vibrational spectroscopy of bulk and supported manganese oxides. Phys Chem Chem Phys 1:185–190 Article CAS Google Scholar

Cao F, Xiang J, Su S, Wang PY, Sun LS, Hu S, Lei SY (2014) The activity and characterization of MnO_x–CeO_2–ZrO_2/γ-Al_2O_3 catalysts for low temperature selective catalytic reduction of NO with NH_3. Che Eng J 243:347–354 Article CAS Google Scholar

Cao F, Xiang J, Su S, Wang PY, Hu S, Sun L (2015) Ag modified Mn-Ce/γ-Al_2O_3 catalyst for selective catalytic reduction of NO with NH_3 at low-temperature. Fuel Process Technol 135:66–72 Article CAS Google Scholar

Chang HZ, Li JH, Chen XY, Ma L, Yang SJ (2012) Effect of Sn on MnO_x–CeO_2 catalyst for SCR of NO_X by ammonia: enhancement of activity and remarkable resistance to SO_2. Catal Commun 27:54–57 Article CAS Google Scholar

Chang HZ, Wu QR, Zhang T, Li MG, Sun XX, Li JH, Duan L, Hao JK (2015) Design strategies for CeO_2-MoO_3 catalysts for DeNOx and Hg^0 oxidation in the presence of HCl: the significance of the surface acid-base properties. Environ Sci Technol 49:12388–12394 Article CAS Google Scholar

Chen ZH, Wang FR, Li H, Yang Q, Wang LF, Li XH (2012) Low-temperature selective catalytic reduction of NO_x with NH_3 over Fe-Mn mixed-oxide catalysts containing $Fe_3Mn_3O_8$ phase. Ind Eng Chem Res 51:202–212 Article CAS Google Scholar

Deng H, Yu YB, Liu FD, Ma JZ, Zhang Y, He H (2014) Nature of Ag species on Ag/γ-Al_2O_3: a combined experimental and theoretical study. ACS Catal 4:2776–2784 Article CAS Google Scholar

Du XS, Gao X, Cui LW, Fu YC, Luo ZY, Cen KF (2012) Investigation of the effect of Cu addition on the SO_2-resistance of a Ce-Ti oxide catalyst for selective catalytic reduction of NO with NH_3. Fuel 92:49–55 Article CAS Google Scholar

Esteves P, Wu Y, Dujardin C, Dongare MK, Granger P (2011) Ceria–zirconia mixed oxides as thermal resistant catalysts for the decomposition of nitrous oxide at high temperature. Catal Today 176:453–457 Article CAS Google Scholar

Ettireddy P, Ettireddy N, Mamedov S, Boolchand P, Smirniotis P (2007) Surface characterization studies of TiO_2 supported manganese oxide catalysts for low temperature SCR of NO with NH_3. Appl Catal B 76:123–134 Article CAS Google Scholar

Fan XP, Li CT, Zeng GM, Gao Z, Chen L, Zhang W, Gao HL (2010) Removal of gas-phase element mercury by activated carbon fiber impregnated with CeO_2. Energy Fuel 24:4250–4254 Article CAS Google Scholar

Fernández-Miranda N, Lopez-Anton MA, Díaz-Somoano M, Martínez-Tarazona MR (2016) Mercury oxidation in catalysts used for selective reduction of NOx (SCR) in oxy-fuel combustion. Chem Eng J 285:77–82 Article CAS Google Scholar

Gu TT, Liu Y, Weng XL, Wang HQ, Wu ZB (2010) The enhanced performance of ceria with surface sulfation for selective catalytic reduction of NO by NH_3. Catal Commun 12:310–313 Article CAS Google Scholar

Gunnarsson F, Granlund MZ, Englund M, Dawody J, Pettersson LJ, Härelind H (2015) Combining HC-SCR over Ag/Al_2O_3 and hydrogen generation over Rh/CeO_2-ZrO_2 using biofuels: an integrated system approach for real applications. Appl Catal B 162:583–592 Article CAS Google Scholar

Guo RT, Zhen WL, Pan WG, Zhou Y, Hong JN, Xu HJ, Jin Q, Ding CG, Guo SY (2014) Effect of Cu doping on the SCR activity of CeO_2 catalyst prepared by citric acid method. J Ind Eng Chem 20:1577–1580 Article CAS Google Scholar

He C, Shen B, Chen J, Cai J (2014) Adsorption and oxidation of elemental mercury over Ce-MnO_x/Ti-PILCs. Sci Technol 48:7891–7898 Article CAS Google Scholar

He YY, Ford ME, Zhu MH, Liu QC, Tumuluri U, Wu ZL, Wachs IE (2016) Influence of catalyst synthesis method on selective catalytic reduction (SCR) of NO by NH_3 with V_2O_5-WO_3/TiO_2 catalysts. Appl Catal B 193:141–150 Article CAS Google Scholar

Hu JL, Ying Q, Wang YG, Zhang HL (2015) Characterizing multi-pollutant air pollution in China: comparison of three air quality indices. Environ Int 84:17–25 Article CAS Google Scholar

Hutson ND, Attwood BC, Scheckel KG (2007) XAS and XPS characterization of mercury binding on brominated activated carbon. Environ Sci Technol 41:1747–1752 Article CAS Google Scholar

Jampaiah D, Ippolito SJ, Sabri YM, Tardio J, Selvakannan P, Nafady A, Reddy BM, Bhargava S (2016) Ceria–zirconia modified MnOx catalysts for gaseous elemental mercury oxidation and adsorption. Catal Sci Technol 6:1792–1803 Article CAS Google Scholar

Jin RB, Liu Y, Wang Y, Cen WL, Wu ZB, Wang HQ, Weng XL (2014) The role of cerium in the improved SO_2 tolerance for NO reduction with NH_3 over Mn-Ce/TiO_2 catalyst at low temperature. Appl Catal B 148–149:582–588 Article CAS Google Scholar

Karami A, Salehi V (2012) The influence of chromium substitution on an iron–titanium catalyst used in the selective catalytic reduction of NO. J Catal 292:32–43 Article CAS Google Scholar

Kim J, Myeong W, Ihm S (2009) Characteristics of CeO_2-ZrO_2 mixed oxide prepared by continuous hydrothermal synthesis in supercritical water as support of Rh catalyst for catalytic reduction of NO by CO. J Catal 263:123–133 Article CAS Google Scholar

Kim JR, Lee KY, Suh MJ, Ihm SK (2012) Ceria–zirconia mixed oxide prepared by continuous hydrothermal synthesis in supercritical water as catalyst support. Catal Today 185:25–34 Article CAS Google Scholar

Kima YJ, Kwona HJ, Nama IS, Choung JW, Kil JK, Kimb HJ, Chac MS, Yeoc GK (2010) High deNO_x performance of Mn/TiO_2. Catal Today 151:244–250 Article CAS Google Scholar

Lee W, Bae GN (2009) Removal of elemental mercury (Hg^0) by nanosized V_2O_5/TiO_2 catalysts. Environ Sci Technol 43:1522–1527 Article CAS Google Scholar

Lee KJ, Kumar PA, Maqbool MS, Rao KN, Song KH, Ha HP (2013) Ceria added Sb-V_2O_5/TiO_2 catalysts for low temperature NH_3 SCR: physico-chemical properties and catalytic activity. Appl Catal B 142–143:705–717 Article CAS Google Scholar

Leitenbur C, Trovarelli A, Llorca J, Cavani F, Bini G (1996) The effect of doping CeO_2 with zirconium in the oxidation of isobutene. Appl Catal A 139:161–173 Article Google Scholar

Li J, Pan YB, Xiang CS, Ge QM, Guo JK (2006) Low temperature synthesis of ultrafine α-Al_2O_3 powder by a simple aqueous sol–gel process. Ceram Int 32:587–591 Article CAS Google Scholar

Li Y, Murphy PD, Wu CY, Powers KW, Bonzongo JCJ (2008) Development of silica/vanadia/titania catalysts for removal of elemental mercury from coal-combustion flue gas. Environ Sci Technol 42:5304–5313 Article CAS Google Scholar

Li JH, Chang HZ, Ma L, Hao JM, Yang RT (2011) Low-temperature selective catalytic reduction of NOx with NH_3 over metal oxide and zeolite catalysts—a review. Catal Today 175:147–156 Article CAS Google Scholar

Li HL, Wu CY, Li Y, Zhang JY (2012) Superior activity of MnOx-CeO_2/TiO_2 catalyst for catalytic oxidation of elemental mercury at low flue gas temperatures. Appl Catal B 111:381–388 Article CAS Google Scholar

Li HL, Wu SK, Li LQ, Wang J, Ma WW, Shih K (2015) CuO–CeO_2/TiO_2 catalyst for simultaneous NO reduction and Hg^0 oxidation at low temperatures. Catal Sci Technol 5:5129–5138 Article CAS Google Scholar

Li SJ, Wang XX, Tan S, Shi Y, Li W (2017) CrO_3 supported on sargassum-based activated carbon as low temperature catalysts for the selective catalytic reduction of NO with NH_3. Fuel 191:511–517 Article CAS Google Scholar

Lian ZH, Liu FD, He H (2014) Enhanced activity of Ti-modified V_2O_5/CeO_2 catalyst for the selective catalytic reduction of NO_x with NH_3. Ind Eng Chem Res 53:19503–19511 Article CAS Google Scholar

Lietti L, Alemany JL, Forzatti P, Busca G, Ramis G, Giamello E, Bregani F (1996) Reactivity of V_2O_5-WO_3/TiO_2 catalysts in the selective catalytic reduction of nitric oxide by ammonia. Catal Today 29:143–148 Article CAS Google Scholar

Liu SW, Zhou JC, Liu RX (2014) Preparation of nano t-ZrO_2 particle by the integrated process of high-gravity field and hydrothermal crystallization. Adv Mater Res 881-883:933–939 Article CAS Google Scholar

Liu YX, Wang Q, Pan JF (2016) Novel process on simultaneous removal of nitric oxide and sulfur dioxide using vacuum ultraviolet (VUV)-activated $O_2/H_2O/H_2O_2$ system in a wet VUV-spraying reactor. Environ Sci Technol 50:12966–12975 Article CAS Google Scholar

Liu YX, Xu W, Pan JF, Wang Q (2017) Oxidative removal of NO from flue gas using ultrasound, Mn^{2+}/Fe^{2+} and heat coactivation of Oxone in an ultrasonic bubble reactor. Chem Eng J 326:1166–1176 Article CAS Google Scholar

Liu YX, Liu ZY, Wang Y, Yin YS, Pan JF, Zhang J, Wang Q (2018) Simultaneous absorption of SO_2 and NO from flue gas using ultrasound/Fe^{2+}/heat coactivated persulfate system. J Hazard Mater 342:326–334 Article CAS Google Scholar

Ludvigsson M, Lindgren J, Tegenfeldt J (2001) Incorporation and characterisation of oxides of manganese, cobalt and lithium into Nafion 117 membranes. J Mater Chem 11:1269–1276 Article CAS Google Scholar

Ma Z, Wu XD, Si ZC, Weng D, Ma J, Xu TF (2015) Impacts of niobia loading on active sites and surface acidity in NbOx/CeO_2-ZrO_2 NH_3-SCR catalysts. Appl Catal B 179:380–394 Article CAS Google Scholar

Madier Y, Descorme C, Le Govic AM, Duprez D (1999) Oxygen mobility in CeO_2 and $Ce_xZr_{(1-x)}O_2$ compounds: study by CO transient oxidation and 18O/16O isotopic exchange. J Phys Chem B 103:10999–11006 Article CAS Google Scholar

Mullins D, Overbury SH, Huntley DR (1998) Electron spectroscopy of single crystal and polycrystalline cerium oxide surfaces. Surf Sci 409:307–319 Article CAS Google Scholar

Prabhakaran T, Mangalaraja RV, Denardin JC, Jimenez JA (2017) The effect of reaction temperature on the structural and magnetic properties of nano $CoFe_2O_4$. Ceram Int 43:5599–5606 Article CAS Google Scholar

Presto AA, Granite EJ (2006) Survey of catalysts for oxidation of mercury in flue gas. Environ Sci Technol 40:5601–5609 Article CAS Google Scholar

Qi GS, Yang RT (2003) Low-temperature selective catalytic reduction of NO with NH_3 over iron and manganese oxides supported on titania. Appl Catal B 44:217–225 Article CAS Google Scholar

Qi GS, Yang RT, Chang RS (2004) MnO_X-CeO_2 mixed oxides prepared by co-precipitation for selective catalytic reduction of NO with NH_3 at low temperatures. Appl Catal B 51:93–106 Article CAS Google Scholar

Qu L, Li CT, Zeng GM, Zhang MY, Fu MF, Ma JF, Zhan FM, Luo DQ (2014) Support modification for improving the performance of MnO_x–CeO_y/r-Al_2O_3 in selective catalytic reduction of NO by NH_3. Chem Eng J 242:76–85 Article CAS Google Scholar

Rallo M, Lopez-Anton M, Contreras ML, Maroto-Valeret M (2012) Mercury policy and regulations for coal-fired power plants. Environ Sci Pollut Res Int 19:1084–1096 Article CAS Google Scholar

Shen BX, Zhang XP, Ma HQ, Yao Y, Liu T (2013) A comparative study of Mn/CeO_2, Mn/ZrO_2 and Mn/Ce-ZrO_2 for low temperature selective catalytic reduction of NO with NH_3 in the presence of SO_2 and H_2O. J Environ Sci 25:791–800 Article CAS Google Scholar

Shen BX, Wang YY, Wang FM, Liu T (2014) The effect of Ce–Zr on NH_3-SCR activity over MnO_x(0.6)/$Ce_{0.5}Zr_{0.5}O_2$ at low temperature. Chem Eng J 236:171–180 Article CAS Google Scholar

Shimizu T (1992) Partial oxidation of hydrocarbons and oxygenated compounds on perovskite oxides. Catal Rev 34:355–371 Article CAS Google Scholar

Su YX, Fan BX, Wang LS, Liu YF, Huang BC, Fu ML, Chen LM, Ye DQ (2013) MnO_x supported on carbon nanotubes by different methods for the SCR of NO with NH_3. Catal Today 201:115–121 Article CAS Google Scholar

Tang XF, Li YG, Huang XM, Xu YD, Zhu HQ, Wang JG, Shen WJ (2006) Manganese-cerium mixed oxide catalysts for complete oxidation of formaldehyde: effect of preparation method and calcination temperature. Appl Catal B 62:265–273 Article CAS Google Scholar

Tang XF, Chen JL, Huang XM, Xu YD, Shen WJ (2008) Pt/MnOx–CeO_2 catalysts for the complete oxidation of formaldehyde at ambient temperature. Appl Catal B 81:115–121 Article CAS Google Scholar

Terribilea D, Trovarellia A, Llorcab J, Leitenburga C, Dolcetti G (1998) The preparation of high surface area CeO_2-ZrO_2 mixed oxides by a surfactant-assisted approach. Catal Today 43:79–88 Article Google Scholar

Trawczyński J, Bielak B, Miśta W (2005) Oxidation of ethanol over supported manganese catalysts—effect of the carrier. Appl Catal B 55:277–285 Article CAS Google Scholar

Wan Q, Duan L, He KB, Li JH (2011) Removal of gaseous elemental mercury over a CeO_2–WO_3/TiO_2 nanocomposite in simulated coal-fired flue gas. Chem Eng J 170:512–517 Article CAS Google Scholar

Wang XH, Lu GZ, Guo Y, Xue YY, Jiang LZ, Guo YL, Zhang ZG (2007) Structure, thermal-stability and reducibility of Si-doped Ce-Zr-O solid solution. Catal Today 126:412–419 Article CAS Google Scholar

Wang HQ, Cao S, Cen CP, Chen XB, Wu ZB (2013) Structure–activity relationship of titanate nanotube-confined ceria catalysts in selective catalytic reduction of NO with ammonia. Catal Lett 143:1312–1318 Article CAS Google Scholar

Wang PY, Su S, Xiang J, You HW, Cao F, Sun LS, Hu S, Zhang Y (2014) Catalytic oxidation of Hg^0 by MnOx–CeO_2/r-Al_2O_3 catalyst at low temperatures. Chemosphere 101:49–54 Article CAS Google Scholar

Wang YY, Shen BX, He C, Yue SJ, Wang FM (2015) Simultaneous removal of NO and Hg^0 from flue gas over Mn–Ce/Ti-PILCs. Environ Sci Technol 49:9355–9363 Article CAS Google Scholar

Wang B, Chi C, Xu M, Wang C, Meng D (2017) Plasma-catalytic removal of toluene over CeO_2-MnO_x catalysts in an atmosphere dielectric barrier discharge. Chem Eng J 322:679–692 Article CAS Google Scholar

Wu ZB, Jiang BQ, Liu Y, Zhao WR, Guan BH (2007) Experimental study on a low-temperature SCR catalyst based on $MnO_{(x)}/TiO_2$ prepared by sol-gel method. J Hazard Mater 145:488–492 Article CAS Google Scholar

Xie GY, Liu ZY, Zhu ZP, Liu QY, Ge J, Huang Z (2004) Simultaneous removal of SO_2 and NO_x from flue gas using a CuO/Al_2O_3 catalyst sorbent: I. Deactivation of SCR activity by SO_2 at low temperatures. J Catal 224:36–41 Article CAS Google Scholar

Xie JK, Yan NQ, Yang SJ, Qu Z, Chen WM, Zhang WQ, Li KH, Liu P, Jia JP (2012) Synthesis and characterization of nano-sized Mn–TiO_2 catalysts and their application to removal of gaseous elemental mercury. Res Chem Intermed 38:2511–2522 Article CAS Google Scholar

Xu WQ, Yu YB, Zhang CB, He H (2008) Selective catalytic reduction of NO by NH_3 over a Ce/TiO_2 catalyst. Catal Commun 9:1453–1457 Article CAS Google Scholar

Xu WQ, He H, Yu YB (2009) Deactivation of a Ce/TiO_2 catalyst by SO_2 in the selective catalytic reduction of NO by NH_3. J Phys Chem C 113:4426–4432 Article CAS Google Scholar

Xu HD, Zhang QL, Qiu CT, Lin T, Gong MC, Chen YQ (2012) Tungsten modified MnO_x-CeO_2/ZrO_2 monolith catalysts for selective catalytic reduction of NO_x with ammonia. Chem Eng Sci 76:120–128 Article CAS Google Scholar

Xu HD, Wang Y, Cao Y, Fang ZT, Lin T, Gong MC, Chen YQ (2014) Catalytic performance of acidic zirconium-based composite oxides monolithic catalyst on selective catalytic reduction of NO_x with NH_3. Chem Eng J 240:62–73 Article CAS Google Scholar

Xu HM, Qu Z, Zong CX, Huang WJ, Quan FQ, Yan NQ (2015) MnOx/graphene for the catalytic oxidation and adsorption of elemental mercury. Environ Sci Technol 49:6823–6830 Article CAS Google Scholar

Yang SJ, Guo YF, Yan NQ, Qu Z, Xie JK, Yang C, Jia JP (2011) Capture of gaseous elemental mercury from flue gas using a magnetic and sulfur poisoning resistant sorbent Mn/γ-Fe_2O_3 at lower temperatures. J Hazard Mater 186:508–515 Article CAS Google Scholar

Yang J, Yang Q, Sun J, Liu QC, Zhao D, Gao W, Liu L (2015) Effects of mercury oxidation on V_2O_5–WO_3/TiO_2 catalyst properties in NH_3-SCR process. Catal Commun 59:78–82 Article CAS Google Scholar

Yang W, Liu YX, Wang Q, Pan JF (2017a) Removal of elemental mercury from flue gas using wheat straw chars modified by Mn-Ce mixed oxides with ultrasonic-assisted impregnation. Chem Eng J 326:169–181 Article CAS Google Scholar

Yang YJ, Liu J, Zhang BK, Zhao YC, Chen XY, Shen FH (2017b) Experimental and theoretical studies of mercury oxidation over CeO_2-WO_3/TiO_2 catalysts in coal-fired flue gas. Chem Eng J 317:758–765 Article CAS Google Scholar

Yang ZQ, Li HL, Liu X, Li P, Yang JP, Lee PH, Shih K (2018) Promotional effect of CuO loading on the catalytic activity and SO_2 resistance of MnOx/TiO_2 catalyst for simultaneous NO reduction and Hg^0 oxidation. Fuel 1:79–88 Article CAS Google Scholar

Yu CL, Huang BC, Dong LF, Chen F, Liu XQ (2017) In situ FT-IR study of highly dispersed MnO_x/SAPO-34 catalyst for low-temperature selective catalytic reduction of NO_x by NH_3. Catal Today 281:610–620 Article CAS Google Scholar

Zhang YP, Zhu XQ, Shen K, Xu HT, Sun KQ, Zhou CC (2012) Influence of ceria modification on the properties of TiO_2–ZrO_2 supported V_2O_5 catalysts for selective catalytic reduction of NO by NH_3. J Colloid Interface Sci 376:233–238 Article CAS Google Scholar

Zhang YP, Guo WQ, Wang LF, Song M, Yang LJ, Shen K, Xu HT, Zhou CC (2015) Characterization and activity of V_2O_5-CeO_2/TiO_2-ZrO_2 catalysts for NH_3-selective catalytic reduction of NO_x. Chin J Catal 36:1701–1710 Article Google Scholar

Zhang Y, Yang JP, Yu XH, Sun P, Zhao YC, Zhang JY, Chen G, Yao H, Zheng CG (2017) Migration and emission characteristics of Hg in coal-fired power plant of China with ultra low

emission air pollution control devices. Fuel Process Technol 158:272–280 Article CAS Google Scholar

Zhao Y, Hao RL, Qi M (2015) Integrative process of preoxidation and absorption for simultaneous removal of SO_2, NO and Hg^0. Chem Eng J 269:159–167 Article CAS Google Scholar

Zhao LK, Li CT, Wang Y, Wu H, Gao L, Zhang J, Zeng GM (2016a) Simultaneous removal of elemental mercury and NO from simulated flue gas using a CeO_2 modified V_2O_5-WO_3/TiO_2 catalyst. Catal Sci Technol 6:6076–6086 Article CAS Google Scholar

Zhao LK, Li CT, Li SH, Wang Y, Zhang JY, Wang T, Zeng GM (2016b) Simultaneous removal of elemental mercury and NO in simulated flue gas over V_2O_5/ZrO_2-CeO_2 catalyst. Appl Catal B 198:420–430 Article CAS Google Scholar

Zhou ZJ, Liu XW, Zhao B, Shao HZ, Xu YS, Xu MH (2016a) Elemental mercury oxidation over manganese-based perovskite-type catalyst at low temperature. Chem Eng J 288:701–710 Article CAS Google Scholar

Zhou ZJ, Liu XW, Liao ZQ, Shao HZ, Lv C, Hu YC, Xu MH (2016b) Manganese doped CeO_2-ZrO_2 catalyst for elemental mercury oxidation at low temperature. Fuel Process Technol 152:285–293 Article CAS Google Scholar